PCCP

Accepted Manuscript

ROYAL SOCIETY OF CHEMISTRY

www.rsc.org/pccp

First-principles examination of conducting monolayer 1T′-MX_2 (M = Mo, W; X = S, Se, Te): Promising catalysts for hydrogen evolution reaction and its enhancement by strain

Darwin Barayang Putungan,[1,2,3] Shi-Hsin Lin,[3,*] and Jer-Lai Kuo[3,†]

[1]*Department of Physics, National Taiwan University, Taipei, Taiwan*

[2]*TIGP Nanoscience and Technology program, Institute of Physics, Academia Sinica, Taipei, Taiwan*

[3]*Institute of Atomic and Molecular Sciences, Academia Sinica, Taipei, Taiwan*

Abstract

We investigated the application of 1T′-MX_2 (M = Mo, W; X = S, Se, Te) 2D materials as hydrogen evolution reaction (HER) catalysts using density functional theory. Our results show that 1T′-MX_2 have lower energies and are dynamically more stable than their 1T counterparts, therefore likely more relevant to previous experimental findings and applications. We found that sulfides are the better catalysts, followed by selenides and tellurides. Specifically, 1T′-MoS_2 and WS_2 are the best HER catalysts among MX_2. We proposed a mechanism, rather than the metallicity surmised previously, based on the calculated density of states. On the other hand, the effectively stretched (compressed) X site of the 1T′ 2×1 reconstruction from 1T is shown to be more (less) active for HER. We further exploited application of external strain to tune and boost HER performance. Our findings are of significance in the elucidation of previous experimental works and exploration of potential materials for clean energy applications.

*Author to whom correspondence should be addressed. Electronic address:slin2@gate.sinica.edu.tw

†Author to whom correspondence should be addressed. Electronic address:jlkuo@pub.iams.sinica.edu.tw

I. INTRODUCTION

Hydrogen evolution reaction (HER) is one key mechanism by which a sustainable production of hydrogen could be achieved [1–3]. Being emission free, hydrogen gas is highly regarded as a clean alternative energy carrier to carbon-based fuels [4]. The strength of hydrogen adsorption on a catalyst has been shown to be a good descriptor of HER, usually expressed in terms of the Gibb's free energy of adsorption [5, 6]. For superior catalytic performance, it should be close to the thermoneutral value of approximately zero, implying moderate H adsorption [7, 8].

Platinum is known to be the most active single-metal catalyst for HER, although its limited availability and high cost hinder the possibility of large-scale hydrogen generation [9–13]. Numerous studies have been carried out to search for potential alternative, mostly on non-precious metals [14–16], nanoparticulate structures [7, 17–19] and recently on single layer two-dimensional (2D) materials known as transition metal dichalcogenides (TMDs) [3, 13, 20–26]. Previous findings utilizing the stable 1H phase TMDs point to the metallic edge sites as the active sites [3, 20, 22, 24, 27] thereby rendering the basal plane as catalytically useless. This limits the HER activity, as the edge sites are few and need to be exposed for maximum efficiency.

Recently, the metallic phase of MoS_2 and WS_2 known as 1T (Mo and W in octahedral coordination) phase has been found to be exceptionally better in terms of HER activity compared to its 1H (Mo and W in trigonal prismatic coordination) counterpart [21, 23, 25, 26, 28], and are comparable to that of platinum's HER performance [23, 25, 26]. (Pt can reach as low as 30 mV/dec while the supposedly 1T MoS_2 and WS_2 can reach as low as 40 mV/dec and 55 mV/dec respectively). In particular, it was suggested that for 1T-MoS_2, the basal plane is active [25]. However, the perfect 1T phase is known to be metastable [29–32], and subsequent findings revealed that such structure is dynamically unstable, and thus cast doubts on its stability [32]. On the other hand, related theoretical and experimental works have suggested that the energetically more stable phase is a distorted 2×1 reconstruction of the 1T phase [29, 32–35]. With reference to 1T-MoS_2, this structure is known as 1T′-MoS_2, and posses a stable phonon spectra [32]. It is therefore of great importance to comprehensively analyze the HER potentials of the 1T′ phase, including the characteristics of basal plane active sites, and hydrogen adsorption mechanism.

In this work, we explored the basal plane HER activity and mechanism of select 1T′-MX_2 (M = Mo, W; X = S, Se, Te), including their dynamical stability and electronic structure. As depicted in Figure 1, the 2 × 1 reconstruction of perfect 1T phase results to two different X sites: one under internal tensile strain (labeled as X_T in Fig. 1(a)), and the other under internal compressive strain (labeled as X_C in Fig. 1(b)). We found that the one under tensile strain is more active in HER, and we showed that further application of tensile strain significantly impacts HER, and can activate inert basal plane sites. Finally, we have identified that sulfides generally show better HER activity compared to their selenides and tellurides counterparts.

II. METHODOLOGY

All calculations were done utilizing spin-polarized density functional theory (DFT) in the generalized gradient approximation (GGA) as implemented in VASP 5.3.5 code [36, 37], with projector-augmented wave method under the Perdew-Burke-Ernzenhof (PBE) [38] exchange-correlation functional. Our calculations also include dispersion corrections by means of the DFT-D3 method as implemented by Grimme [39–41], in order to correct for the instantaneous charge fluctuations that are usually neglected in conventional exchange-correlation functionals. To obtain 1T′ phase, following the method employed by Hu, Li and Dong [29], we constructed a rectangular supercell from 1T phase as the initial structure to break the symmetry. The structure was then relaxed to final 1T′ structure. This was done for all 1T′-MX_2 (M = Mo, W; X = S, Se, Te) 2D materials. A vacuum space of 20 Å was used to separate each slab to avoid inter-layer interaction. A cut off energy of 550 eV was used throughout all calculations, and positions of atoms were relaxed until the forces on each atom is below 0.01 eV/Å, with the above-mentioned vacuum spacing fixed. Brillouin zone integration is carried out using a 5 ×5 × 1 k-point mesh. In order to look into the dynamical stability of the 1T′ structures, phonon dispersions were calculated by Phonopy [42] using force constants obtained from density functional perturbation theory (DFPT) [43] as implemented in VASP. The stability of hydrogen adsorption is described by hydrogen adsorption energy $\Delta E_{\text{ads, H}}$ defined by

$$\Delta E_{\text{ads, H}} = E_{\text{1T′-MX}_2\text{ + H}} - E_{\text{1T′-MX}_2} - \frac{1}{2}E_{\text{H}_2}, \quad (1)$$

where $E_{1T'\text{-}MX_2\,+\,H}$ is the total energy of 1T′-MX_2 with adsorbed hydrogen atom, $E_{1T'\text{-}MX_2}$ is the total energy of the 1T′-MX_2 monolayer, and E_{H_2} is the energy of a gas phase hydrogen molecule. The Gibbs free energy of adsorption $\Delta G_{\text{ads, H}}$ is then calculated via

$$\Delta G_{\text{ads, H}} = \Delta E_{\text{ads, H}} + \Delta E_{\text{ZPE}} - T\Delta S_{\text{H}}, \tag{2}$$

where ΔE_{ZPE} is the difference in zero-point energy of hydrogen in adsorbed and gas phase, and ΔS_{H} is the entropy difference between the adsorbed state and gas phase of hydrogen. This term is usually approximated as $\Delta S_{\text{H}} \approx \frac{1}{2} S_{H_2}$ [13, 24, 26, 44]. Here, S_{H_2} is the entropy of gas phase H_2 at standard condition (300 K). Our working hydrogen coverage on the basal plane is $\frac{1}{16}$. Variation of $\Delta G_{\text{ads, H}}$ under tensile biaxial strain is investigated as well for all 1T′-MX_2 monolayers. As our tests show that vibrational frequencies are not sensitive to strain (only 2 meV ZPE correction difference for 0% and 8% strain), we used the same corrections as for the pristine (0% strain case) for each specific strained 1T′-MX_2.

III. RESULTS AND DISCUSSIONS

This section starts with the discussion of structural parameters, energetics, phonon stability and electronic structures of 1T′-MX_2 (M = Mo, W; X = S, Se, Te) 2D materials (Section III A). Section III B presents Gibbs free energy of hydrogen adsorption on various basal plane sites, and their characterization. Finally, the sensitivity of Gibbs free energy under tensile biaxial strain is discussed in Section III C.

A. 1T′-MX_2 (M = Mo, W; X = S, Se, Te) monolayers

We first describe the structural properties of 1T′-MX_2 monolayers. Fig. 1 shows a representative optimized geometrical configuration of the 1T and 1T′ phases, particularly for MoS_2. The resulting Mo dimerization strips can be viewed from the top view (Fig. 1(b)) while the clustering of Mo atoms can be clearly seen from the side view (Fig. 1(b)). The basic unit cell $a_0^{'} \times b_0^{'}$ for the 1T′ structure is also indicated in Figure 1(b), which is approximately equivalent to the $a_0 \times 2a_0$ superlattice (where $b_0^{'} \approx 2a_0$) of 1T phase reported in previous works [29, 32–35] as the lowest energy superstructure of the 1T′ phase. This is also equivalent to the rectangular $a_0 \times \sqrt{3}a_0$ structure [35]. These two unit cells give rise

to 2 × 1 reconstruction and zigzag distortion of M atoms in 1T′-MX_2 as can be seen in the figure. The $a_0^{'}$ × $b_0^{'}$ lattice parameters for 1T′-MX_2 (M = Mo, W; X = S, Se, Te) are listed in Table I.

TABLE I: Optimized unit cell parameters of 1T′-MX_2 monolayers. The lattice parameters $a_0^{'}$, $b_0^{'}$ and $\theta^{'}$ are defined in Figure 1(b).

1T′-MX_2	$a_0^{'}$	$b_0^{'}$	$\theta^{'}$
MoS_2	3.14	6.48	119.0
$MoSe_2$	3.24	6.74	118.77
$MoTe_2$	3.38	7.17	118.11
WS_2	3.16	6.49	119.13
WSe_2	3.26	6.74	118.98
WTe_2	3.45	7.14	118.86

To assess the relative energetic stabilities of the 1H, 1T, and 1T′ phases, we calculated the energy per formula unit (per MX_2). Our calculations suggest that 1T′ phase is always lower in energy compared to 1T in the order of several hundreds of meV, in exact agreement with the previous work [33]. Starting from sulfides to selenides and finally to tellurides, 1T′ phase becomes more stabilized with respect to 1T. On the other hand, the 1H phase is the most stable phase for all MX_2, except for WTe_2, in which the distorted 1T′ phase is the lowest energy structure and consistent with experimental studies [45]. It is known experimentally that in the case of MoS_2, the 1T phase reverts back to its original trigonal prismatic phase upon heating (at around 300^0 C) or aging. [46]. Meanwhile, in a recent theoretical study, the 1T phases of all considered MX_2 were found to be dynamically not stable [47]. For example, the calculated imaginary frequency of 1T-MoS_2 was found to be as high as ≈ 280 cm^{-1} [32]. We thus further confirmed the dynamical stability of 1T′-MX_2 2D materials by calculating phonon dispersions (see Fig. S1 and the corresponding discussion in Supplementary Information). Meanwhile, the obtained phonon frequencies agree well with the Raman spectra results [23].

Besides being stable, the electrode materials have to be able to conduct currents. Therefore we calculated their band structures (Fig. S2 in Supplementary Information). The results shows that 1T′-MX_2, either being metals or small gap semiconductors ($\approx$ 0.10-0.15 eV), are

suitable for electrode applications. Hence in this section we have demonstrated that 1T′-MX_2 are more stable than 1T-MX_2 and, in the mean time, appropriate electrode materials. We addressed their applicability for HER in the next section.

B. Hydrogen adsorption on basal plane sites

HER is a two-step reaction [7] that can be written, in totality, as

$$H^+ + e^- \rightarrow \frac{1}{2}H_2, \tag{3}$$

The initial state is the combination of a proton and an electron, intermediate state is an adsorbed H atom on the electrode, and final state is a hydrogen molecule. These can be described by the following reactions:

$$H^+ + e^- + * \rightarrow H^*, \tag{4}$$

$$2H^* \rightarrow H_2, \text{or } H^+ + e^- + H^* \rightarrow H_2, \tag{5}$$

where the * denotes an adsorption site on the surface, and H* denotes adsorbed hydrogen on an adsorption site.

Following Nørskov's analyses [7, 8], $\Delta G_{\text{ads, H}}$ between the intermediate and final states can be calculated and has been demonstrated to be a useful descriptor for HER. A catalyst is appropriate for HER if $\Delta G_{\text{ads, H}}$ is close to thermoneutral, that is $\Delta G_{\text{ads, H}} \approx 0$. There are two distinct adsorption sites on 1T′-MX_2 due to the 2 $\times$ 1 reconstruction. One X site (denoted as X_T site in Fig. 1) has longer M-X bond lengths, which is equivalent to the effect of a tensile strain, while the other X site (labeled as X_C site in Fig. 1) has shorter M-X bonds equivalent to the effect of a compressive strain. In this work, we calculated $\Delta G_{\text{ads, H}}$ for all 1T′-MX_2 X_T and X_C sites.

As shown in Fig. 2, $\Delta G_{\text{ads, H}}$ is lower and closer to zero on X_T site compared to X_C site among all 1T′-MX_2 materials, implying that HER activity is better on the tensile-strained site. Moreover, 1T′ sulfides generally exhibit lower $\Delta G_{\text{ads, H}}$ and thus translates to better HER performance, followed by selenides and finally tellurides. This finding is similar to the observed trend for 1H phase of MX_2 [13]. Our calculations predict 1T′-MoS_2 to be the most effective HER catalyst, with 1T′-WS_2 coming next. These findings agree with previous experimental works [25, 26], wherein the samples were thought to be

1T phase with the basal plane being the active sites. We, however, found that 1T-MX_2 with hydrogen adsorbed undergoes a 2×1 reconstruction (see Fig. 1(c)) and relaxes to 1T′ [32]. Therefore, 1T′ can be the more experimentally relevant phase for HER, and our present results provide a very first comprehensive DFT calculation to demonstrate the HER performance of the 1T′ structure. As presented in Section I, Pt is the most active catalyst for HER and operates at full hydrogen coverage [27]. The interaction of hydrogen with Pt has been extensively investigated through various experimental techniques such as temperature programmed desorption and thermal desorption spectroscopy [48, 49], and also through density functional calculations [50, 51]. In comparison with Pt, the HER performance of these select 1T'-MX_2 has been found to be comparable to Pt, experimentally (see Section I), and now computationally as described by our calculated Gibbs free energy of adsorption. We further showed that applying strain can bring these materials' HER activity closer to that of Pt. This will be presented in detail in Section III C. As discussed in the following paragraph, we also found that the mechanism to interact with H atom for these 1T'-MX_2 is similar to that of Pt [50], although the responsible state here is not a pure *d*-band, but a hybridized *p*-*d* band.

To analyze HER mechanism on 1T′-MX_2, we analyzed the projected density of states (PDOS) of these materials before and after hydrogen adsorption. Fig. 3 shows the atomic PDOS of the X_T site together with that of hydrogen atom. For all MX_2, states near the Fermi level (X_T *p* states) diminished upon hydrogen adsorption (labeled as X_T-H *p* states in Fig. 3), and, in the mean time, hydrogen *s* states above and below Fermi level are formed. Those X_T site *p* states near Fermi level are responsible for hybridizing with H 1*s* states, resulting to bonding and anti-bonding states. If the energy splitting between the formed bonding and anti-bonding states are large enough such that the anti-bonding states can be shifted above Fermi level (as can be seen from H 1*s* discussed above), the energy of the system is then lowered, making the adsorption favored. Therefore, the more states participating in the hybridization near the Fermi level, the greater the energy benefit is and thus leads to better hydrogen adsorption. This feature of PDOS can be correlated to our calculated $\Delta G_{\mathrm{ads,\,H}}$(Fig. 2). The main peaks of hydrogen's anti-bonding states shift to lower energies as we traverse from sulfides to selenides and finally to tellurides. It indicates decreasing energy splittings between bonding and anti-bonding states and hence the adsorption energies. Moreover, the number of X_T *p* states of pristine MX_2 that is diminished within -2 eV to 0 eV

(as done by numerical integrations of the differences of the projected PDOS without and with hydrogen adsorption) decreases slightly from sulfides to selenides, and to tellurides. The same is true for the X_C site (Supplementary Information Fig. S3), with lower anti-bonding H 1s states and less diminished states near the Fermi level than the X_T site. These explain the observed HER activity inferiority of X_C site compared to X_T site.

We believe that the states near Fermi level that is involved in the hybridization is a more relevant descriptor of HER activity than the metallicity proposed in recent works on TMD monolayers [3, 20, 22, 24, 27]. Similar discussions for transition metal catalysts can be found in Ref. [52, 53]. It was found that not all candidate metallic catalysts are effective [52, 54]. Noted here, metallicity implies the existence of states near Fermi level, however, these states are not necessarily be able to participate in the hybridization, as can be inferred from the PDOS. To conclude this section, we showed that 1T′-MoS_2 and 1T′-WS_2 emerge as excellent HER catalysts rather than their selenides and tellurides counterparts, and it is consistent with recent experiments of metallic MoS_2 and WS_2[25, 26].

C. Tensile Biaxial Strain and Gibbs Free Energy

As noted in previous discussions, the effectively tensile-strained X_T site adsorbs hydrogen stronger than the compressive-strained X_C site. We thus further explored the idea of applying external strains to tune and boost the HER efficiency. Strain engineering has been widely adopted to tune the physical and chemical properties of 2D materials[26, 55], thanks to the strength and flexibility of 2D materials. We analyzed the variation in $\Delta G_{\mathrm{ads,\,H}}$ under biaxial tensile strain of up to 8% for all 1T′-MX_2. As evident in Fig. 4, biaxial tensile strain lowers $\Delta G_{\mathrm{ads,\,H}}$ on X_T site and thus improves hydrogen adsorption significantly, especially for sulfides and selenides. For the case of MoS_2, a modest 2% strain dropped $\Delta G_{\mathrm{ads,\,H}}$ to approximately zero which is the best value being sought for these potential HER catalysts. Interestingly, WS_2 appears to be catching up with MoS_2 and eventually becomes better at strains above 3% but reverts back to the original trend after 4% strain. $MoSe_2$ and WSe_2 becomes significantly active for HER after 6% strain. In contrast, there is a moderate drop in $\Delta G_{\mathrm{ads,\,H}}$ for $MoTe_2$ and WTe_2, around 0.48 eV and 0.53 eV from 0% to 8% strain respectively. The same trend is exhibited by X_C sites of 1T′-MX_2, lowering $\Delta G_{\mathrm{ads,\,H}}$ by more than 50%. It is interesting to note that X_C site of $MoTe_2$ becomes significantly active for

strains higher than 6%, with $\Delta G_{\mathrm{ads,\,H}}$, much lower than that of its X_T site. For larger strain, $\Delta G_{\mathrm{ads,\,H}}$ can be several tens to hundreds of meV below zero, implying stronger hydrogen adsorption. Since hydrogen adsorption becomes weaker for higher hydrogen coverage, $\Delta G_{\mathrm{ads,\,H}}$ can approach zero at higher coverage and hence higher overall HER efficiency.

Biaxial tensile strain strengthens hydrogen adsorption by reinforcing states near the Fermi level for better interaction with that of hydrogen 1s. Fig. 5 shows the PDOS evolution for the X_T site of a representative 1T′-MX_2 (1T′-MoS_2) for strain values of 0% to 8%. There is a substantial enhancement of states near the Fermi level as further strain is applied. Comparing the PDOS before and after the adsorption, we found that the states participating in the hydrogen binding near Fermi level is also enhanced. Focusing on 8% strain, it can be seen in Fig. 5 that considerable states disappeared from X_T 3p states after hydrogen adsorption compared to 0% in Fig. 5. In the mean time, hydrogen bonding and anti-bonding states positions did not change appreciably with strain, and thus the energy splittings for different strains are approximately the same. Therefore, the stronger adsorption for larger strain is attributed to the enhanced PDOS below Fermi level. As it has been reported recently that, for single-layer MoS_2, strain of up to 11% can be sustained [56], our result can be of immediate experimental relevance. Similar reports argued that the same is true for other TMD 2D materials and nanotubes [57–59]. Subsequently, strain engineering of these 1T′ materials could pave the way for a controllable HER activity on basal plane that could be of importance in advanced applications.

IV. CONCLUSIONS

In summary, we used DFT to investigate HER activity on basal plane of 1T′-MX_2 (M = Mo, W; X = S, Se, Te) 2D materials. Our results show that these single-layer materials have lower energies and are dynamically more stable than their 1T counterparts, therefore likely more relevant to previous experimental findings and applications. They are also shown to be appropriate electrode materials as their electronic structure character lies within the semi-metal and narrow-gap semiconductor regime. We found that distortion in the 1T′ structure results to tensile-strained more active and compressive-strained less active sites. We observed a general trend that in terms of $\Delta G_{\mathrm{ads,\,H}}$, sulfides are better compared to selenides and tellurides, with MoS_2 and WS_2 garnering the closest values to thermoneutral

at 0.15 eV and 0.28 eV respectively. We further exploited the application of tensile strain to improve hydrogen adsorption. $\Delta G_{\mathrm{ads,\,H}}$ is reduced by reinforcing states near the Fermi level for better interaction with hydrogen. We found that MoS_2 and WS_2 basal plane active sites can be fully activated at above 2% strain, while $MoSe_2$ and WSe_2 at above 6% strain. Noteworthy, higher hydrogen coverage can be achieved if larger strain is applied. Thus, we are proposing a tensile strain-based tuning of HER activity on 1T′-MX_2 basal plane as a cheap alternative to rare and expensive catalyst such as platinum. Our findings are of significance in the exploration of potential materials for clean energy applications.

After finalizing our results, we were aware of very recent HER studies on 1T′-MoS_2 monolayer, done by Gao, et al [60] and Fan, et al [61]. The edge site activity of 1T′-MoS_2 was discussed in Ref. [60], and both the edge sites and basal-plane sites were discussed in Ref.[61]. Our findings on MoS_2 stability and reactivity are in agreement with their results. Our results on other 1T′-MX_2 and the corresponding density of states analysis render a systematic trend, an integrated picture of HER using 1T′ TMDs, and an unified mechanism throughout 1T′ TMDs. These results could be useful to future studies utilizing 1T′-MX_2 monolayers for HER and other catalytic reactions.

Acknowledgments

This work was financially supported by various grants from Academia Sinica and the Ministry of Science and Technology (MOST) of Taiwan under MOST101-2113-M-001-023-MY3. D. B. P. would like to thank Taiwan International Graduate Program for scholarship. Computational resources are supported in part by the National Center for High Performance Computing. We wish to thank Yun-Wen Chen and Cheng-Chau Chiu for helpful discussions.

[1] J. A. Turner, *Science*, 2004, **305**, 972–974.

[2] N. S. Lewis, *Nature*, 2001, **414**, 589–590.

[3] Y. Yan, B. Xia, Z. Xu and X. Wang, *ACS Catal.*, 2014, **4**, 1693–1705.

[4] S. Dunn, *Int. J. Hydrogen Energy*, 2002, **27**, 235–264.

[5] B. Hinnemann, P. G. Moses, J. Bonde, K. P. Jorgensen, J. H. Nielsen, S. Horch, I. Chorkendorff and J. K. Nørskov, *J. Am. Chem. Soc.*, 2005, **127**, 5308–5309.

[6] J. K. Nørskov, T. Bligaard, J. Rossmeisl and C. H. Christensen, *Nat. Chem.*, 2009, **1**, 37–46.

[7] J. K. Nørskov, T. Bligaard, A. Logadottir, J. R. Kitchin, J. G. Chen, S. Pandelov and U. Stimming, *J. Electrochem. Soc.*, 2005, **152**, J23.

[8] J. Greeley, T. F. Jaramillo, J. Bonde, I. B. Chorkendorff and J. K. Nørskov, *Nat. Mater.*, 2006, **5**, 909–913.

[9] W. Sheng, H. A. Gasteiger and Y. Shao-Horn, *J. Electrochem. Soc.*, 2010, **157**, B1529.

[10] I. A. Pašti, N. M. Gavrilov and S. V. Mentus, *Adv. Phys. Chem.*, 2011, **2011**, 1–8.

[11] Y. Zheng, Y. Jiao, Y. Zhu, L. H. Li, Y. Han, Y. Chen, A. Du, M. Jaroniec and S. Z. Qiao, *Nat. Commun.*, 2014, **5**, 3783.

[12] Z.-Y. Zhou, N. Tian, Z.-Z. Huang, D.-J. Chen and S.-G. Sun, *Faraday Discuss.*, 2008, **140**, 81–92; discussion 93–112.

[13] H. Pan, *Sci. Rep.*, 2014, **4**, 5348.

[14] J. Deng, P. Ren, D. Deng, L. Yu, F. Yang and X. Bao, *Energy Environ. Sci.*, 2014, **7**, 1919.

[15] Q. Lu, G. S. Hutchings, W. Yu, Y. Zhou, R. V. Forest, R. Tao, J. Rosen, B. T. Yonemoto, Z. Cao, H. Zheng, J. Q. Xiao, F. Jiao and J. G. Chen, *Nat. Commun.*, 2015, **6**, 6567.

[16] M. Tavakkoli, T. Kallio, O. Reynaud, A. G. Nasibulin, C. Johans, J. Sainio, H. Jiang, E. I. Kauppinen and K. Laasonen, *Angew. Chemie Int. Ed.*, 2015, **54**, 4535–4538.

[17] Y. Liu, G.-d. Li, L. Yuan, L. Ge, H. Ding, D. Wang and X. Zou, *Nanoscale*, 2015, 3130–3136.

[18] H. Fei, Y. Yang, Z. Peng, G. Ruan, Q. Zhong, L. Li, E. L. G. Samuel and J. M. Tour, *ACS Appl. Mater. Interfaces*, 2015, **7**, 8083–8087.

[19] E. J. Popczun, C. G. Read, C. W. Roske, N. S. Lewis and R. E. Schaak, *Angew. Chemie - Int. Ed.*, 2014, **53**, 5427–5430.

[20] C. Tsai, K. Chan, F. Abild-Pedersen and J. K. Nørskov, *Phys. Chem. Chem. Phys.*, 2014, **16**, 13156–64.

[21] X. Sun, J. Dai, Y. Guo, C. Wu, F. Hu, J. Zhao, X. Zeng and Y. Xie, *Nanoscale*, 2014, **6**, 8359–67.

[22] H. Wang, Z. Lu, S. Xu, D. Kong, J. J. Cha, G. Zheng, P.-C. Hsu, K. Yan, D. Bradshaw, F. B. Prinz and Y. Cui, *Proc. Natl. Acad. Sci. U. S. A.*, 2013, **110**, 19701–6.

[23] M. A. Lukowski, A. S. Daniel, F. Meng, A. Forticaux, L. Li and S. Jin, *J. Am. Chem. Soc.*, 2013, **135**, 10274–10277.

[24] C. Tsai, F. Abild-Pedersen and J. K. Nørskov, *Nano Lett.*, 2014, **14**, 1381–1387.

[25] D. Voiry, M. Salehi, R. Silva, T. Fujita, M. Chen, T. Asefa, V. B. Shenoy, G. Eda and M. Chhowalla, *Nano Lett.*, 2013, **13**, 6222–6227.

[26] D. Voiry, H. Yamaguchi, J. Li, R. Silva, D. C. B. Alves, T. Fujita, M. Chen, T. Asefa, V. B. Shenoy, G. Eda and M. Chhowalla, *Nat. Mater.*, 2013, **12**, 850–855.

[27] T. F. Jaramillo, K. P. Jørgensen, J. Bonde, J. H. Nielsen, S. Horch and I. Chorkendorff, *Science*, 2007, **317**, 100–102.

[28] U. Maitra, U. Gupta, M. De, R. Datta, A. Govindaraj and C. N. R. Rao, *Angew. Chemie - Int. Ed.*, 2013, **52**, 13057–13061.

[29] T. Hu, R. Li and J. Dong, *J. Chem. Phys.*, 2013, **139**, 174702.

[30] Y.-C. Lin, D. O. Dumcenco, Y.-S. Huang and K. Suenaga, *Nat. Nanotechnol.*, 2014, **9**, 391–6.

[31] A. N. Enyashin, L. Yadgarov, L. Houben, I. Popov, M. Weidenbach, R. Tenne, M. Bar-Sadan and G. Seifert, *J. Phys. Chem. C*, 2011, **115**, 24586–24591.

[32] M. Calandra, *Phys. Rev. B - Condens. Matter Mater. Phys.*, 2013, **88**, 1–7.

[33] K.-A. N. Duerloo, Y. Li and E. J. Reed, *Nat. Commun.*, 2014, **5**, 1–9.

[34] A. P. Nayak, T. Pandey, D. Voiry, J. Liu, S. T. Moran, A. Sharma, C. Tan, C.-H. Chen, L.-J. Li, M. Chhowalla, J.-f. Lin, A. K. Singh and D. Akinwande, *Nano Lett.*, 2015, **15**, 346–353.

[35] R. Gordon, D. Yang, E. Crozier, D. Jiang and R. Frindt, *Phys. Rev. B*, 2002, **65**, 1–9.

[36] G. Kresse and J. Hafner, *Phys. Rev. B*, 1993, **47**, 558–561.

[37] G. Kresse, *Phys. Rev. B*, 1996, **54**, 11169–11186.

[38] J. P. Perdew, K. Burke and M. Ernzerhof, *Phys. Rev. Lett.*, 1997, **78**, 1396–1396.

[39] S. Grimme, *Wiley Interdiscip. Rev. Comput. Mol. Sci.*, 2011, **1**, 211–228.

[40] J. Moellmann and S. Grimme, *J. Phys. Chem. C*, 2014, **118**, 7615–7621.

[41] W. Reckien, F. Janetzko, M. F. Peintinger and T. Bredow, *J. Comput. Chem.*, 2012, **33**, 2023–2031.

[42] A. Togo, F. Oba and I. Tanaka, *Phys. Rev. B*, 2008, **78**, 134106.

[43] S. Baroni, S. De Gironcoli, A. Dal Corso and P. Giannozzi, *Rev. Mod. Phys.*, 2001, **73**, 515–562.

[44] E. Skulason, V. Tripkovic, M. E. Bjorketun, S. Gudmundsdottir, G. Karlberg, J. Rossmeisl, T. Bligaard, H. Jonsson and J. K. Nørskov, *J. Phys. Chem. C*, 2010, **114**, 22374.

[45] M. N. Ali, J. Xiong, S. Flynn, J. Tao, Q. D. Gibson, L. M. Schoop, T. Liang, N. Haldolaarachchige, M. Hirschberger, N. P. Ong and R. J. Cava, *Nature*, 2014, **514**, 5–10.

[46] D. Yang, S. J. Sandoval, W. M. R. Divigalpitiya, J. C. Irwin and R. F. Frindt, *Phys. Rev. B*, 1991, **43**, 12053–12056.

[47] C. Ataca, H. ahin and S. Ciraci, *J. Phys. Chem. C*, 2012, **116**, 8983–8999.

[48] S. K. Jo, *Surf. Sci.*, 2015, **635**, 99–107.

[49] K. Christmann, G. Ertl and T. Pignet, *Surf. Sci.*, 1976, **54**, 365–392.

[50] B. Hammer and J. Nørskov, *Surf. Sci.*, 1995, **343**, 211–220.

[51] Y. Liu, W. Cen, G. Feng, Y. Chu, D. Kong and H. Yin, *Appl. Surf. Sci.*, 2014, **313**, 424–431.

[52] B. Hammer and J. Nørskov, *Adv. Catal.*, 2000, **45**, 71–129.

[53] J. K. Nørskov, F. Abild-Pedersen, F. Studt and T. Bligaard, *Proc. Natl. Acad. Sci. U. S. A.*, 2011, **108**, 937–943.

[54] E. Santos, P. Quaino and W. Schmickler, *Phys. Chem. Chem. Phys.*, 2012, **14**, 11224.

[55] C.-H. Chang, X. Fan, S.-H. Lin and J.-L. Kuo, *Phys. Rev. B*, 2013, **88**, 195420.

[56] S. Bertolazzi, J. Brivio and A. Kis, *ACS Nano*, 2011, **5**, 9703–9709.

[57] M. Ghorbani-Asl, N. Zibouche, M. Wahiduzzaman, A. F. Oliveira, A. Kuc and T. Heine, *Sci. Rep.*, 2013, **3**, 2961.

[58] M. Ghorbani-Asl, S. Borini, A. Kuc and T. Heine, *Phys. Rev. B.*, 2013, **87**, 1–6.

[59] I. Kaplan-Ashiri, S. R. Cohen, K. Gartsman, V. Ivanovskaya, T. Heine, G. Seifert, I. Wiesel, H. D. Wagner and R. Tenne, *Proc. Natl. Acad. Sci. U. S. A.*, 2006, **103**, 523–528.

[60] G. Gao, Y. Jiao, F. Ma, Y. Jiao, E. Waclawik and A. Du, *J. Phys. Chem. C*, 2015, **119**, 13124–13128.

[61] X.-L. Fan, Y. Yang, P. Xiao and W.-M. Lau, *J. Mater. Chem. A*, 2014, **2**, 20545–20551.

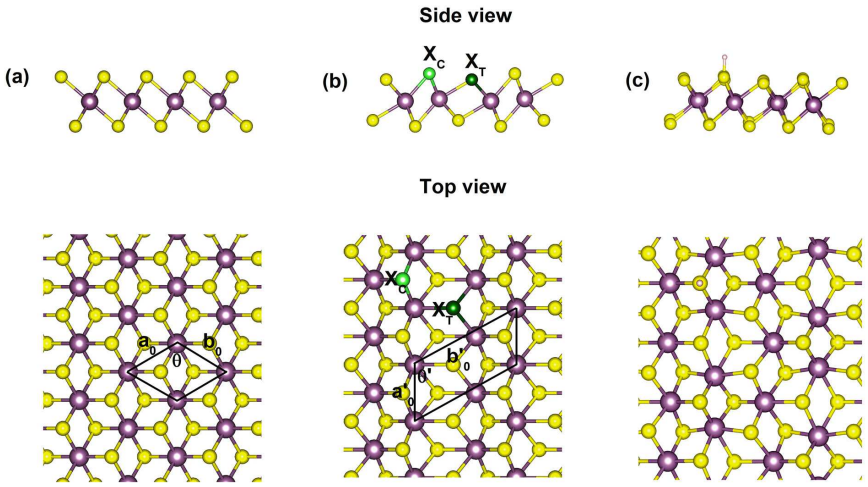

FIG. 1: Structural configuration of (a) perfect 1T and (b) distorted 1T′ phases for 1T′-MoS_2. The respective unit cells are shown for each phase. For 1T′, two distinct adsorption sites appear: the tensile-strained sulfur site we refer to as X_T site (shown as dark green sphere) and the compressive-strained sulfur site denoted as X_C site (shown as light green sphere). In general, X_T and X_C sites also refer to selenium and tellurium atoms for non-sulfide 1T′-MX_2. As such, these X_T and X_C sites can be referenced as adsorption positions and constituent atoms at the same time. Also shown in (c) is the resulting structural reconstructions upon H adsorption on the perfect 1T phase that leads to 1T′ transition.

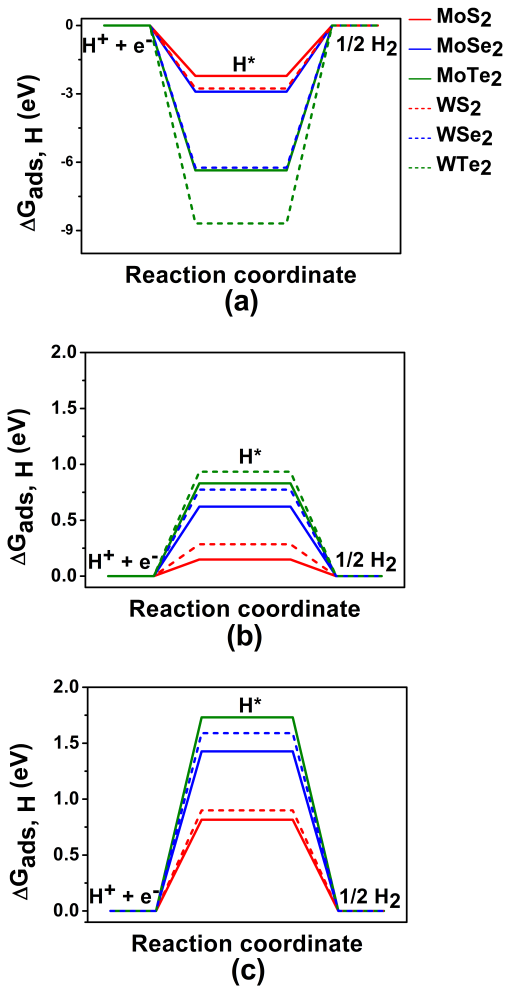

FIG. 2: Calculated $\Delta G_{\mathrm{ads,\,H}}$ of hydrogen adsorption on (a) perfect 1T phase X, (b) 1T′ phase X_T and (c) 1T′ X_C phase sites. The tensile-strained X_T site adsorbs hydrogen better than the X_C site, as manifested by lower $\Delta G_{\mathrm{ads,\,H}}$ for all 1T′ 2D materials.

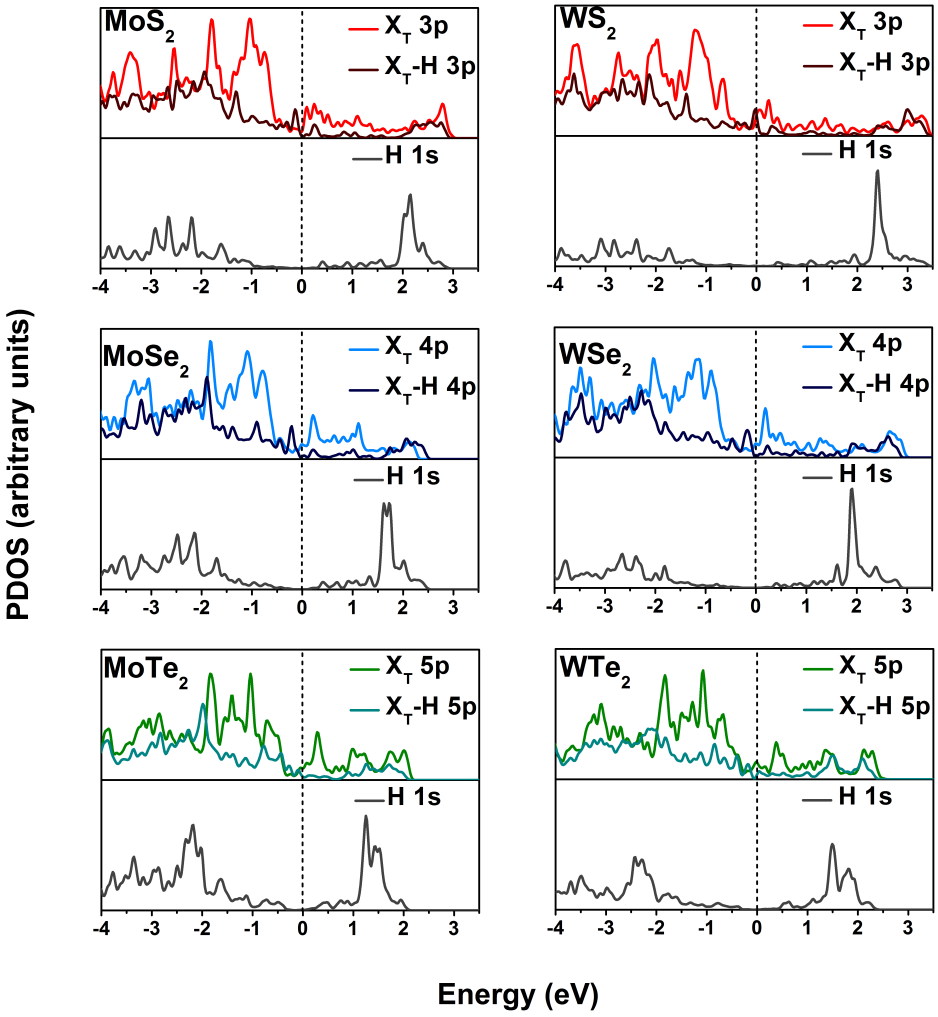

FIG. 3: PDOS plots of 1T′-MX_2 (M = Mo, W; X = S, Se, Te) monolayers projected to different X_T sites before and after hydrogen adsorption. PDOS of H 1s are scaled up by a factor of five for better visualization. States near the Fermi level disappear after hydrogen adsorption, and in the meantime hydrogen 1s state splits into bonding and anti-bonding states. The amount of diminished states near the Fermi level, combined with the magnitude of hydrogen 1s splitting, determine the strength of hydrogen adsorption.

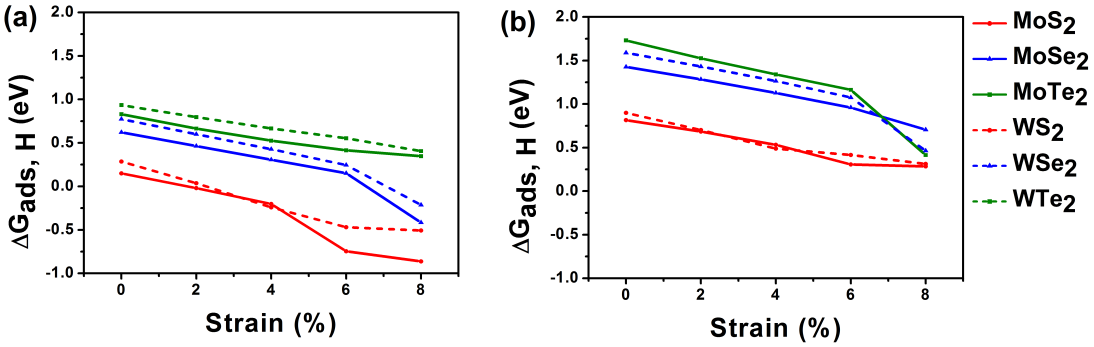

FIG. 4: Variation of $\Delta G_{\text{ads, H}}$ on (a) X_T and (b) X_C sites under different biaxial tensile strain values. Biaxial tensile strain lowers $\Delta G_{\text{ads, H}}$ and improves hydrogen adsorption significantly, notably for sulfides and selenides.

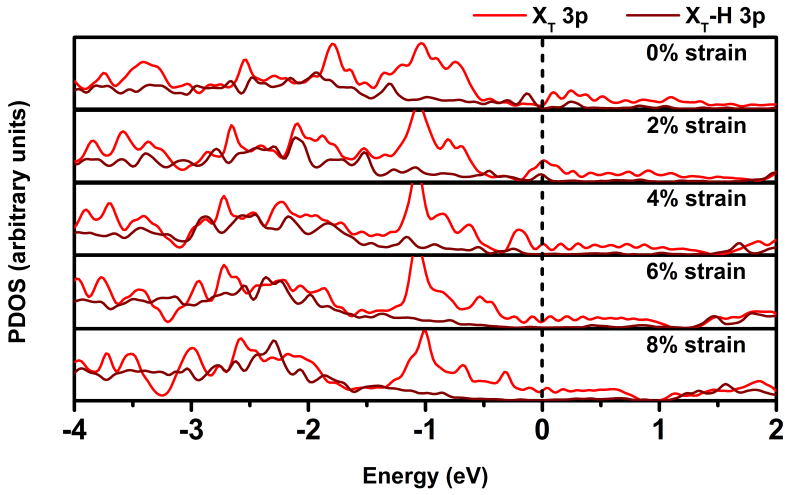

FIG. 5: PDOS Evolution of 1T′-MoS_2 X_T site subject to varying biaxial tensile strain before and after H adsorption. It can be observed that biaxial strain reinforces states near the Fermi level for better interaction with hydrogen $1s$ and thereby strengthening hydrogen adsorption.